

## Charm (and Beauty) Production at the Tevatron

Jonas Rademacker on behalf of the CDF and the DØ Collaboration  
*University of Bristol, H H Wills Physics Laboratory, Bristol, BS8 1TL, UK*

We present recent results on heavy flavour production at Tevatron Run II for typically  $\sim 1 \text{ fb}^{-1}$  of analysed  $p\bar{p}$  data at  $\sqrt{s} = 1.96 \text{ TeV}$ . This includes results on single and correlated open charm and bottom cross sections, charm pair production kinematics,  $J/\psi$ ,  $\psi(2S)$  and  $\chi_{cJ}$  cross sections and polarisation measurements in  $J/\psi$ ,  $\psi(2S)$ ,  $\Upsilon(1S)$ , and  $\Upsilon(2S)$ .

### I. INTRODUCTION

The large  $b\bar{b}$  and  $c\bar{c}$  cross section at  $\sqrt{s} = 1.96 \text{ TeV}$   $p\bar{p}$  makes the Tevatron a unique place for the study of the production and decay of heavy flavour. Already in Run I, heavy flavour production measurements challenged theory, finding heavy flavour production cross sections significantly higher than predicted by Next-to-Leading-Order (NLO) QCD calculations (see for example [1] and [2]). The discrepancy between data and theory was particularly dramatic in the quarkonium production, where the ‘‘Colour Singlet Model’’ leading-order QCD calculation underestimates the measured cross section by more than an order of magnitude (see e.g.[3]).

Since the first hadroproduction measurements in Run I, a number of theoretical advances have been made. Fixed-Order Next to Leading Logarithm (FONLL) calculations [4], describe the open charm and  $b$  production cross sections well. Competing models have been put forward that describe the observed quarkonium production rates and  $p_T$  spectra well, but disagree on their results for quarkonium polarisation.

There has also been dramatic experimental progress. In Run II, which started in 2001, the Tevatron collides  $p$  and  $\bar{p}$  at unprecedented luminosity and energy, and the DØ and the CDF experiment have undergone significant upgrades, many of them optimising the detector for flavour physics. In this paper, we summarise the heavy flavour production measurements in Run II at DØ and CDF, and compare them with theoretical predictions.

As we will see below, heavy flavour production at hadron colliders is a vibrant field which is lead by experiment rather than theory. A particular challenge for theory is the quarkonium polarisation, for which we present new results from the Tevatron in this paper.

All numbers, unless accompanied by a reference to a journal publication, are preliminary.

### II. THE TEVATRON, CDF AND DØ

#### A. The Tevatron Run II

The Tevatron in Run II collides protons and antiprotons at a centre of mass energy of 1.96 TeV with a bunch crossing every 396 ns at each interaction point. Some of the bunches are by design empty, so while the detectors have to be able to cope with peak rates of 2.5 MHz, the average collision rate is  $\sim 1.7 \text{ MHz}$ . Since the start of data taking, the Tevatron has delivered more than  $3 \text{ fb}^{-1}$  of integrated luminosity at each interaction point, and is now reaching peak luminosities of typically  $2 \cdot 10^{32} \text{ cm}^{-2}\text{s}^{-1}$ , with the best runs exceeding  $2.8 \cdot 10^{32} \text{ cm}^{-2}\text{s}^{-1}$ . Two general purpose detectors take data at the Tevatron, CDF and DØ. Both collaborations have analysed approximately  $1 \text{ fb}^{-1}$  of nearly  $3 \text{ fb}^{-1}$  each has on tape.

#### B. The CDF and DØ Detectors

Both the CDF and the DØ collaboration have a strong heavy flavour physics programme, and in the last upgrade many features have been added to the detectors to facilitate this programme. These features include precise vertexing, extended  $\mu$  coverage, and sophisticated read-out electronics and triggers. A description of the DØ detector can be found at [5] and of the CDF detector at [6].

The same detector characteristics that make DØ and CDF powerful B physics experiments, also provide the basis for a wide-ranging charm physics programme. The feature that makes DØ stand out as a heavy flavour experiment particularly is its large  $\mu$  coverage [7], up to  $|\eta| < 2$ . CDF’s most distinctive detector element for B and charm physics is its fully hadronic track trigger [8].

#### C. Triggers

Once every 396 ns there is a bunch crossing at each Tevatron interaction point, typically resulting in a very busy event; only a few tens of a per mill (ca  $6 \cdot 10^{-4}$  at CDF) of those events can be written to tape and analysed in detail, the vast majority will be

discarded instantly. The trigger is crucial, and has to operate in a challenging environment. There are two basic strategies to trigger on heavy flavour events.

- Trigger on leptons ( $\mu, e$ ). This provides a clean signature in a hadronic environment, where most tracks are pions. Both experiments use this strategy.  $D\bar{O}$  benefits particularly from its large  $\mu$  coverage, giving large number of semileptonic and leptonic B and charm events, as well as charmonium and bottomium decays, e.g. 180k  $J/\psi$  in the first  $0.1 \text{ fb}^{-1}$ , and 28k  $B \rightarrow J/\psi K$  in  $1.6 \text{ fb}^{-1}$  (after selection cuts).
- Trigger on the long lifetimes of B and D mesons. This is very challenging in a hadronic environment because it requires very fast track and impact parameter reconstruction in very busy events, in time for the trigger decision. Both experiments use this strategy. But only CDF's displaced track trigger has enough bandwidth to trigger on fully hadronic decays alone, while  $D\bar{O}$  have to require an additional lepton in the event to keep the trigger rates manageable. This high-bandwidth displaced track trigger gives CDF unique access to fully hadronic heavy flavour decays, such as 13M  $D^0 \rightarrow K^- \pi^+$  events (here, and in similar expressions in the rest of the note, the charge-conjugate decay is always implied), 0.3M  $D_s^+ \rightarrow \phi(K^+ K^-) \pi^+$  event as well as 53k  $B_s \rightarrow D_s^\pm \pi^\mp$  in  $\sim 1 \text{ fb}^{-1}$  [9] (numbers after selection cuts).

### III. CROSS SECTIONS

#### A. D and B production cross sections

Amongst the earliest Tevatron Run II results were heavy flavour cross section measurements. Figure 1 shows CDF's measurement of the prompt differential charm production cross section versus  $p_T$  for  $|\eta| < 1$ , for  $D^0, D^+, D^{*+}$  and  $D_s$  mesons. Using only  $5.8 \text{ pb}^{-1}$ , less than 0.5% of the presently analysed dataset, the statistical error, given by the inner error bars, is already smaller than the systematic uncertainty; the combined statistical and systematic uncertainty is given by the outer error bars. The uncertainty on the FONLL calculation [11] is given as the grey band, with the central value shown as a solid line. While the measured cross sections appear to be consistently higher than the FONLL prediction, the results are compatible within the (correlated) errors.

The analyses use the reconstructed impact parameter of the D to distinguish prompt D mesons (with zero impact parameter) from those originating from B decays (with large impact parameters).

The same technique of using either impact parameters or decay length has been used to measure inclu-

$p_t^{\min} =$	Ratio: measurement/NLO-prediction in 2006			
	6-7 GeV	10GeV	15GeV	$\sim 20 \text{ GeV}$
channel				
$b + \bar{b}$ jets			$1.2 \pm 0.3$	$1.0 \pm 0.3$
$\mu + b$ jet		$1.5 \pm 0.2$		
$\mu^+ + \mu^-$	$3.0 \pm 0.6$			
$\mu^+ + \mu^-$	$2.3 \pm 0.8$			

TABLE I: Ratios of measurements and predictions for correlated  $b\bar{b}$  cross section measurements, presented by F. Happacher at DIS 2006 [18]. New (2007) results from CDF in the  $\mu^+ \mu^-$  channel are presented in here. (Table taken from [18], slightly modified.)

sive B cross sections in  $B \rightarrow D^0 \mu^+ \nu X$ ,  $B \rightarrow D^{*-} \mu^+ \nu X$  and  $B \rightarrow J/\psi X$  decays, where long decay lengths or large impact parameters identify  $D^0 \mu$ ,  $D^{*-} \mu$  and  $J/\psi$  originating from B mesons. The inclusive differential cross sections measured in the  $D^0 \mu$ ,  $D^{*-} \mu$  and the  $J/\psi$  channel are shown in Figures 2 and 3. The results are in good agreement with FONLL calculations. The preliminary result for the integrated inclusive B cross section for  $b$ -hadrons with  $p_t > 9 \text{ GeV}$  and  $|y| < 0.6$  is:

$$\sigma(p\bar{p} \rightarrow H_b) = 1.34 \mu\text{b} \pm 0.08 \mu\text{b}(\text{stat})_{-0.14}^{+0.13} \mu\text{b}(\text{sys}) \pm 0.07 \mu\text{b}(\text{BR})$$

for the analysis using  $H_b \rightarrow D^0(K^- \pi^+) \mu X$ , and

$$\sigma(p\bar{p} \rightarrow H_b) = 1.47 \mu\text{b} \pm 0.18 \mu\text{b}(\text{stat})_{-0.19}^{+0.17} \mu\text{b}(\text{sys}) \pm 0.11 \mu\text{b}(\text{BR})$$

for the analysis using  $H_b \rightarrow D^{*+}(D^0(K^- \pi^+) \pi^+) \mu X$ , where  $H_b$  stands for a generic  $b$  hadron. The last uncertainty is due to the uncertainty in the branching fractions of the specific final states of the  $D^0$  and  $D^*$  being investigated. The result is in good agreement with the FONLL value of  $1.39_{-0.34}^{+0.49} \mu\text{b}$  [17].

CDF performed a measurement of the exclusive  $B^+ \rightarrow J/\psi K^+$  measurement, using  $0.74 \text{ fb}^{-1}$ , finding  $\sigma(p_t > 6 \text{ GeV}, |y| < 1) = (2.65 \pm 0.12(\text{stat}) \pm 0.21(\text{sys})) \mu\text{b}$  [12]. The differential cross sections for the exclusive measurement can be seen in Fig 2 together with the  $B \rightarrow J/\psi X$  inclusive results. All measurements disagree significantly with NLO calculations. The agreement with FONLL is however very good.

#### B. Correlated $b\bar{b}$ and $c\bar{c}$ cross sections

For correlated  $b\bar{b}$  and  $c\bar{c}$  cross sections, i.e. cross sections where both the quark and the antiquark are within a certain, central rapidity range, higher order terms are expected to be smaller and consequently NLO calculations are expected to describe the data

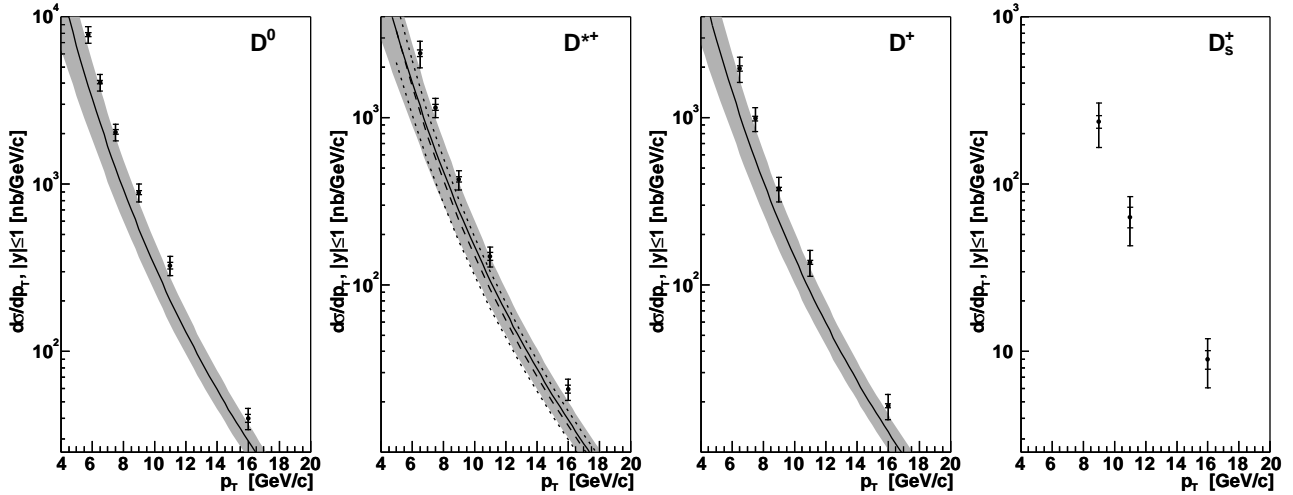


FIG. 1: Differential charm cross section measured in fully hadronic charm decays using only  $5.8 \text{ pb}^{-1}$  at CDF ([10]). The inner error bars represent the statistical uncertainty, the outer error bars represent the total uncertainty of the measurement, and the black line and grey band the central value and uncertainty of the FONLL calculation by [11]. No calculation for the  $D_s$  cross section was available at the time.

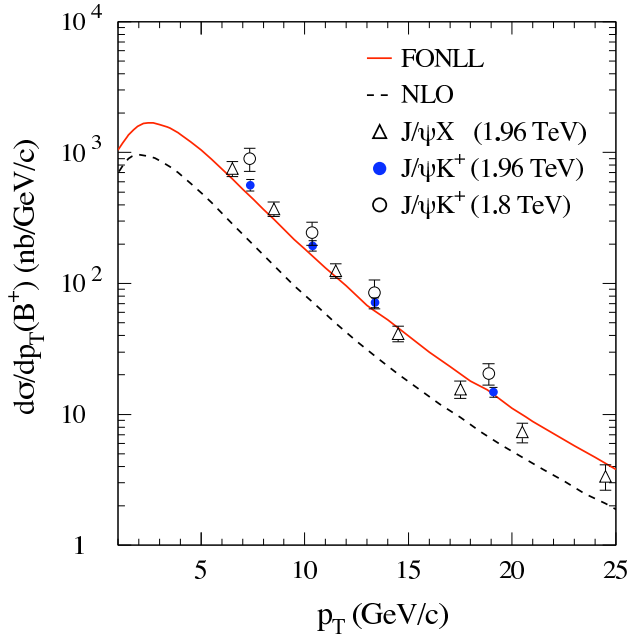


FIG. 2: Comparing inclusive  $B \rightarrow J/\psi X$  [6] and exclusive  $B^+ \rightarrow J/\psi K^+$  [12] cross section measurements, with Run I results [13], NLO [14, 15] and FONLL [4, 16] predictions.

better [18, 19]. In the past, Tevatron results on correlated  $b\bar{b}$  cross sections have been inconclusive. Table I shows the status presented by [18] at DIS 2006. Especially in the  $\mu^+\mu^-$  channel, results have been at odds with NLO predictions. This year (2007) CDF have presented a new measurement of the correlated  $b\bar{b}$  and  $c\bar{c}$  cross section in the  $\mu^+\mu^-$  channel, based on  $0.74 \text{ fb}^{-1}$ . The study uses  $\mu^+\mu^-$  pairs with transverse

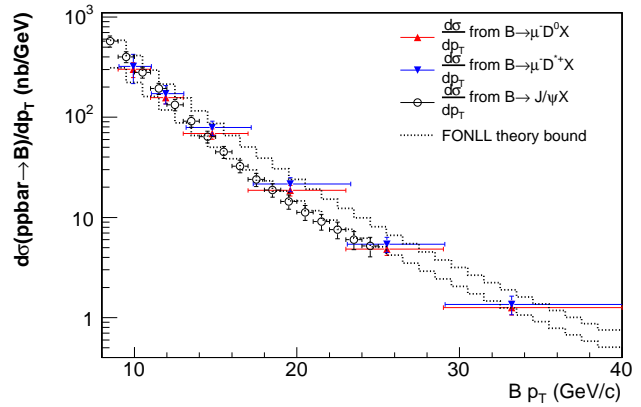


FIG. 3: Comparing inclusive  $B \rightarrow D\mu\nu X$  with inclusive  $B \rightarrow J/\psi X$  [6] and the FONLL calculation by [17].

momentum  $p_T > 3 \text{ GeV}$ , pseudorapidity  $|\eta| < 0.7$  and invariant mass  $m_{\mu\mu} \in [5, 80] \text{ GeV}$ . This corresponds to  $b\bar{b}$  pairs with  $p_T \geq 2 \text{ GeV}$  and a rapidity  $|y| \leq 1.3$ . Prompt  $\mu$  are separated from  $\mu$  created in charm decays, and those from  $\mu$  created in  $B$  decays, using the impact parameters of each muon in the  $\mu^+\mu^-$  pair. The 1-D projection of the impact parameter distribution, and fit, is shown in Fig 4.

The preliminary result for the correlated  $b\bar{b}$  production cross section, where each  $b$  quark decays to a  $\mu$ , is

$$\sigma_{b \rightarrow \mu, \bar{b} \rightarrow \mu} = (1549 \pm 133) \text{ pb.}$$

and for  $c\bar{c}$  production where each charm quark decays to a  $\mu$  is

$$\sigma_{c \rightarrow \mu, \bar{c} \rightarrow \mu} = (624 \pm 104) \text{ pb}$$

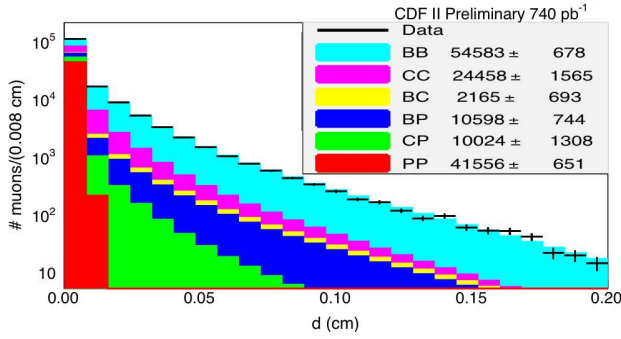


FIG. 4: Impact parameter ( $d$ ) distribution of  $\mu^+\mu^-$  pairs. Although only the projection onto 1 dimension is shown, the fit is performed on the full 2-D distribution of  $\mu^+$  and  $\mu^-$  impact parameters. The different letter combinations that can be found in the legend distinguish muon pairs from B (“BB”), from charm (“CC”), and prompt pairs (“PP”) and various mixtures, such as “BP” where one muon is prompt and the other from a B decay.

	$\epsilon = 0.006$	$\epsilon = 0.002$
$\frac{\sigma_{b \rightarrow \mu \bar{b} \rightarrow \mu}^{\text{measured}}}{\sigma_{b \rightarrow \mu \bar{b} \rightarrow \mu}^{\text{NLO}}}$	$1.2 \pm 0.2$	$1.0 \pm 0.2$
$\frac{\sigma_{c \rightarrow \mu \bar{c} \rightarrow \mu}^{\text{measured}}}{\sigma_{c \rightarrow \mu \bar{c} \rightarrow \mu}^{\text{NLO}}}$	$2.7 \pm 0.6$	$1.6 \pm 0.4$

TABLE II: Measured correlated  $b\bar{b}$  and  $c\bar{c}$  cross sections in  $0.74 \text{ fb}^{-1}$  at CDF, divided by NLO predictions, for different assumptions for the Peterson fragmentation parameter  $\epsilon$  [20].

Translating the  $b \rightarrow \mu$ ,  $\bar{b} \rightarrow \mu$  cross section to an inclusive  $b\bar{b}$  cross section, independent of the final state:

$$\sigma_{b\bar{b}}(p_T \geq 6 \text{ GeV}, |y| \leq 1) = (1618 \pm 148 \pm [\sim 400 \text{ fragmentation}]) \text{ nb}$$

where the dominant error comes from the uncertainty in the fragmentation function, i.e. the fraction of  $b$  quarks that decay to  $\mu$ . Different values for the Peterson fragmentation parameter  $\epsilon$  [20] result in significantly different results, especially for the correlated  $c\bar{c}$  cross section. This can be seen in Table II, where the ratio of the measured cross sections and the NLO predictions is given for two values of the Peterson fragmentation parameter  $\epsilon$ . The value traditionally used,  $\epsilon = 0.006$ , is obtained from fits to  $e^+, e^-$  data [21]. However, [16] point out that these calculations, made on the basis of LO parton level cross sections evaluated with the leading-log approximation of the parton shower event generator, cannot be consistently used with exact NLO calculations, and find that a more suitable value of the Peterson fragmentation parameter would be  $\epsilon = 0.002$ . For  $b\bar{b}$  the results for both values of  $\epsilon$  are now in good agreement with NLO predictions, in contrast to previous measurements. For  $c\bar{c}$

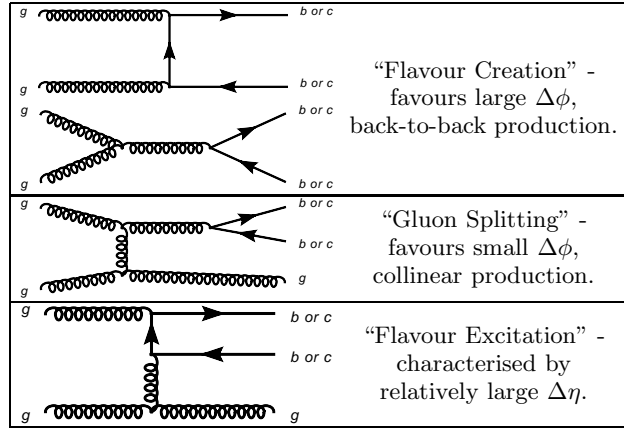


FIG. 5: Heavy flavour production mechanisms in  $p\bar{p}$  collisions. Different mechanisms lead to different kinematics.

the agreement between measurement and NLO prediction depends crucially on the choice of  $\epsilon$ , and no firm statements regarding the compatibility between CDF’s correlated  $c\bar{c}$  cross section measurement and NLO calculations can be made until the issue of a suitable fragmentation parameter is resolved.

#### IV. CHARM PAIR CROSS SECTION

Different production mechanisms for heavy flavour quark-antiquark pairs lead to different kinematic distributions. The leading production mechanism, and their kinematic signature, are depicted in Fig 5. The lowest order diagrams (“Flavour Creation”) favours back-to-back production of the quark-antiquark pair, while “Gluon Splitting” favours collinear production. Measuring the angular distribution in charm pair production therefore gives clues about the  $c\bar{c}$  production mechanism.

Figure 6 shows the  $D^0, D^{*-}$  pair cross section and the  $D^+, D^{*-}$  pair cross section as a function of the angle between the two charm mesons, for the kinematic range  $|y^{D^0}| < 1$ ,  $p_T^{D^0} \in [5.5, 20] \text{ GeV}$  and  $|y^{D^*}| < 1$ ,  $p_T^{D^*} \in [5.5, 20] \text{ GeV}$ . Using a  $D^*$  in the reconstruction ensures clean data samples. It can be seen that in both cases, collinear production is approximately of the same size as back-to-back production. The figure also shows the result from the Pythia event generator, configured to run with leading order matrix elements plus parton shower (Tune A). The total pair production cross sections agree well between the Pythia simulation and the data. However, the simulation over-estimates back-to-back production and under-estimates collinear production.

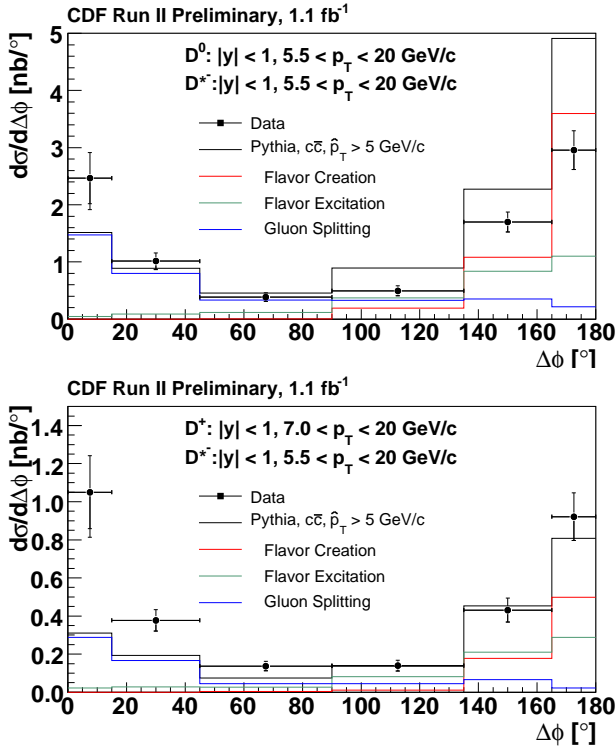


FIG. 6:  $D^0, D^*$  pair cross section and  $D^+, D^*$  pair cross section as a function of the azimuthal angle between the to charm mesons (dots with error bars). The black line shows the result from the Pythia event generator [22], run with leading order matrix elements + parton shower, tune A [23, 24, 25, 26]. The coloured lines show the contribution to the simulated events from different production mechanisms.

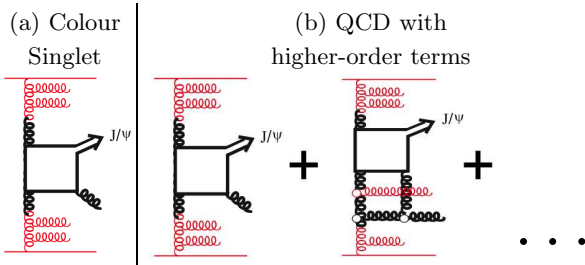


FIG. 7: “Colour singlet” lowest order QCD (left), and QCD with higher order terms (right). The hard scattering process is shown in bold. The higher order terms considered are those where the “bleaching gluon” is absorbed by one of the parton spectators [27].

## V. CHARMONIUM, BOTTOMIUM

Producing a colour-neutral  $J^P = 1^-$  state directly by gluon-gluon fusion is not possible. The simplest solution to the problem is to produce a colour-charged  $c\bar{c}$  (or  $b\bar{b}$ ) pair with gluon fusion and “bleach” it by radiating off a gluon. The “colour-singlet” mecha-

nism, illustrated in Fig 7 (a), was first used to describe quarkonium production [28, 29], but dramatically fails to describe the observed data at the Tevatron, underestimating the  $J/\psi$  and  $\psi'$  production in Run I by more than an order of magnitude (see e.g. [30]). The discussion about a solution to this problem is dominated by two approaches:

- The “Colour Octet” mechanism proposed by [31] is an effective field theory model based on Non-Relativistic QCD (NRQCD). It combines results from [32] and elements of the Colour Evaporation model (CEM). The CEM was originally proposed in [33, 34]; more recent discussions can be found in [35, 36]. In the CEM the  $J/\psi$  is essentially formed in a coloured state, so no “bleaching gluon” is needed. Then the colour “evaporates” in the emission of soft gluons.
- [27] perform a calculation based on full, relativistic QCD, adding higher-order terms to the colour singlet term of the type shown in Fig 7(b), where the “bleaching gluon” is absorbed by a spectator parton. Although each additional term is small, there is such a large number of such diagrams that the sum of them does indeed make a large enough contribution to account for the order-of-magnitude difference between the observed cross sections and those predicted by the colour-singlet model.

Both NRQCD colour-octet and higher-order perturbative QCD describe the observed  $J/\psi$  and  $\psi'$  cross sections and  $p_t$  spectra well (see for example [27, 31, 37]), where the NRQCD approach has a number of adjustable hadronisation parameters that allow a certain level of tuning. However, NRQCD makes a firm prediction that the  $J/\psi$  should be transversely polarised [38] while perturbative QCD predicts a longitudinal polarisation of the  $J/\psi$  [27].

The  $k_t$  factorisation approach [39, 40, 41, 42, 43, 44, 45, 46, 47], can be combined with the colour singlet and the colour octet mechanism. In contrast to the usual collinear approach,  $k_T$  factorisation takes the non-vanishing transverse momentum of the interacting gluons into account when calculating the hadronic matrix element. Especially when combined with the colour-octet mechanism, it describes the production cross sections well, although there is a number of adjustable parameters that are not yet fixed by experimental data [45, 46]. In contrast to the usual NRQCD colour-octet mechanism,  $k_T$  factorisation predicts a longitudinal polarisation of the quarkonium that increases with  $p_T$ .

For a more complete and detailed review of the theory of quarkonium production at hadron colliders, including comparison to data, see [48] and references therein.

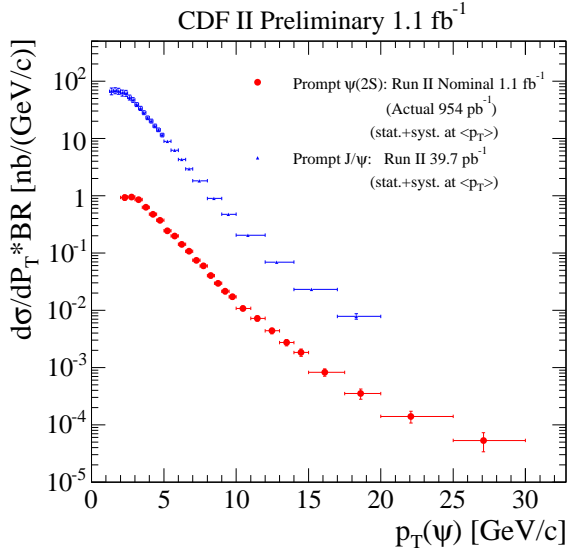


FIG. 8: Differential cross section of prompt  $\psi(2S)$  cross section in  $\sim 1 \text{ fb}^{-1}$ , with an earlier result for the  $J/\psi$  cross section [6] superimposed.

### A. The $\psi(2S)$ Cross Section

The differential cross section of prompt  $\psi(2S)$  from  $\sim 1 \text{ fb}^{-1}$  at CDF Run II and, for comparison the differential cross section of prompt  $J/\psi$  from  $39.7 \text{ pb}$  at CDF Run II is shown in Fig 8. The preliminary result for the integrated cross section of  $p\bar{p} \rightarrow \psi(2S)X$  at  $\sqrt{s} = 1.96 \text{ TeV}$ , with a subsequent decay  $\psi(2S) \rightarrow \mu^+\mu^-$ , in the kinematic range  $|y_{\psi(2S)}| < 0.6, p_T > 2 \text{ GeV}$ , is

$$\begin{aligned} & \sigma(p\bar{p} \rightarrow \psi(2S)X, |y_{\psi(2S)}| < 0.6, p_T > 2 \text{ GeV}) \\ & \times Br(\psi(2S) \rightarrow \mu^+\mu^-) \\ & = (2.60 \pm 0.05(stat)_{-0.18}^{+0.19}(syst)) \text{ nb} \end{aligned}$$

### B. Measurement of charmonium polarisation

The  $J/\psi$  can have three polarisation states, two transverse and one longitudinal. In  $J/\psi \rightarrow \mu^+\mu^-$  decays, the transverse and longitudinal polarisation states can be disentangled by measuring the angle  $\theta^*$  between the  $J/\psi$  and the  $\mu^+$  in the the  $J/\psi$  restframe. It is useful to define the parameter  $\alpha$  in terms of the cross section of transversely polarised  $J/\psi$ ,  $\sigma_T$ , and the cross section of longitudinally polarised  $J/\psi$ ,  $\sigma_L$ , as:

$$\alpha \equiv \frac{\sigma_T - 2\sigma_L}{\sigma_T + 2\sigma_L} \quad (1)$$

If the one longitudinal and the two transverse polarisation states are all equally populated, one would measure  $\alpha = 0$ ; for longitudinal polarisation,  $\alpha < 0$ , and

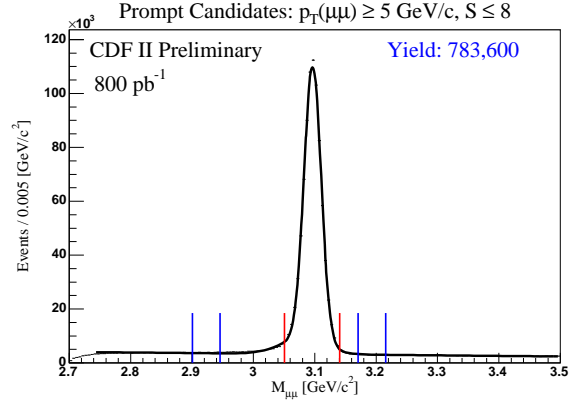


FIG. 9: Invariant mass of  $\mu^+\mu^-$  pairs at CDF (after selection cuts). CDF finds  $0.78M$  prompt  $J/\psi$  in  $0.8 \text{ fb}^{-1}$  [49].

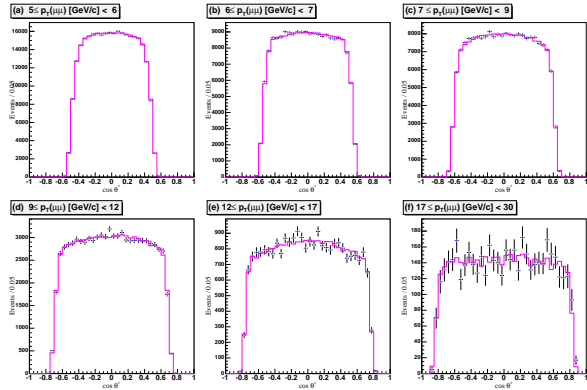


FIG. 10: The measured  $\cos \theta^*$  distribution in different momentum bins for prompt  $J/\psi$  in  $0.8 \text{ fb}^{-1}$  at CDF. The  $p_T$  bins are from left to right, top to bottom:  $[5 - 6]$ ,  $[6 - 7]$ ,  $[7 - 9]$ ,  $[9 - 12]$ ,  $[12 - 17]$ ,  $[17 - 30]$  GeV. A flat distribution indicates no polarisation, a concave (U) distribution transverse polarisation and a convex ( $\cap$ ) distribution longitudinal polarisation.

for transverse polarisation,  $\alpha > 0$ . The parameter  $\alpha$  can be extracted from the distribution of events as a function of  $\cos \theta^*$ :

$$\frac{dN}{d(\cos \theta^*)} \propto 1 + \alpha \cos^2 \theta^* \quad (2)$$

In  $0.8 \text{ fb}^{-1}$ , CDF finds  $0.8M$  prompt  $J/\psi \rightarrow \mu^+\mu^-$  decays. The mass distribution of the  $\mu^+\mu^-$  pairs is shown in Fig 9.  $J/\psi$  originating from B decays are rejected using an impact parameter cut. The  $\cos \theta^*$  distributions are analysed in six bins of different  $p_T$ , as shown in Fig 10. The result in terms of the parameter  $\alpha$  as a function of  $p_T$  is shown in Fig 11 (a). The plot shows  $p_T$ -dependent, longitudinal polarisation of the prompt  $J/\psi$ . This contradicts NRQCD which predicts increasingly transverse polarisation with higher momenta;  $k_T$  factorisation on the other hand appears to over-estimate the longitudinal polarisation. The

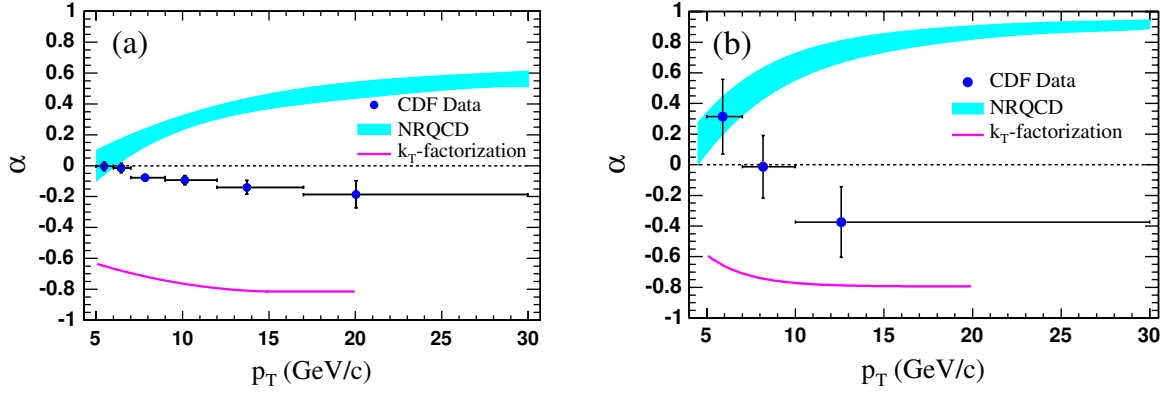


FIG. 11: The polarisation parameter  $\alpha$  vs momentum for prompt  $J/\psi$ (a) and prompt  $\psi(2S)$  (b) at CDF [49]. Negative  $\alpha$  correspond to longitudinal polarisation, positive  $\alpha$  to transverse polarisation. The NRQCD calculation [38, 50, 51] is superimposed in turquoise, the  $k_T$  factorisation calculation [46] in magenta.

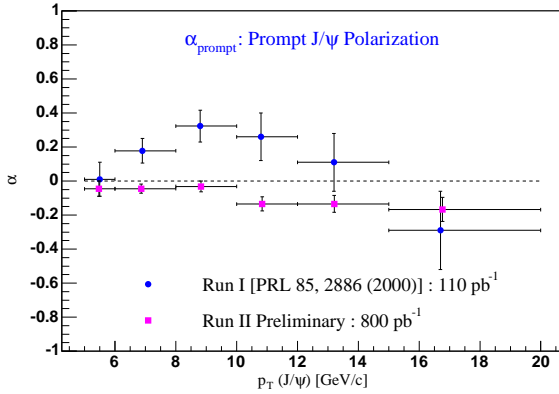


FIG. 12: The polarisation parameter  $\alpha$  vs momentum for prompt  $J/\psi$  at CDF Run I and Run II, where the Run II data were re-analysed to match the binning in Run I.

result also disagrees with Run I results for  $110 \text{ pb}^{-1}$  at a centre-of-mass energy of 1.8 TeV, where evidence of positive polarisation of the  $J/\psi$  was seen. To facilitate a comparison between the Run I and Run II results, the Run II results have been re-analysed using the same binning as in Run I. The comparison is shown in Fig 12.

The polarisation has also been measured in the theoretically cleaner (no feed down from higher states)  $\psi'$  channel; the result is shown in Fig 11 (b). The event numbers are much lower than for the  $J/\psi$  but the results indicate a trend for the longitudinal polarisation fraction to increase with higher  $p_T$ , inconsistent with the NRQCD calculation. These results have been published in [49].

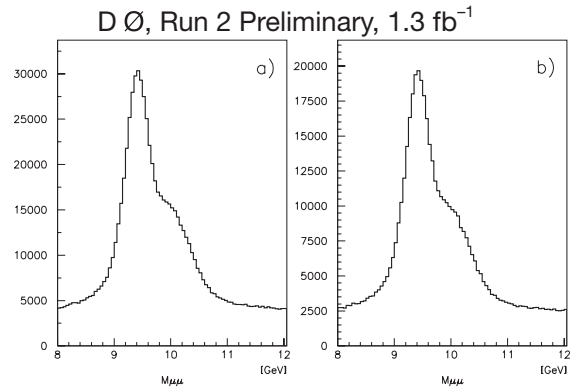


FIG. 13: The  $\mu^+\mu^-$  mass distribution at  $D^0$  after selection cuts, on the left for all events, on the right only for those events selected by the di-muon trigger.

## VI. MEASUREMENT OF THE $\Upsilon$ POLARISATION

The theoretical methods describing the production and polarisation of  $\Upsilon(1S)$  and  $\Upsilon(2S)$  in  $p-\bar{p}$  collisions are equivalent to those for charmonium presented in the previous section.

The  $D^0$  experiment measures the polarisation of the  $\Upsilon(1S)$  and the  $\Upsilon(2S)$  as a function of the  $\Upsilon$  transverse momentum in  $1.3 \text{ fb}^{-1}$  of data in Tevatron Run II. Data are selected in the di-muon channel. To achieve a more reliable estimate of the trigger efficiency in the cross section calculation, only events selected by the di-muon trigger are used in the analysis. The invariant mass of the  $\mu^+\mu^-$  pairs near the  $\Upsilon$  mass is shown in Fig 13 for all data passing the selection cut (a), and those that also were selected by the di-muon trigger (b). Figure 14 shows the di-muon mass spectrum for one bin in  $|\cos\theta^*|$  and  $p_T$ , with the fit to the data superimposed, and the Gaussians describing the individual contribution of the  $\Upsilon(1S)$ ,  $\Upsilon(2S)$

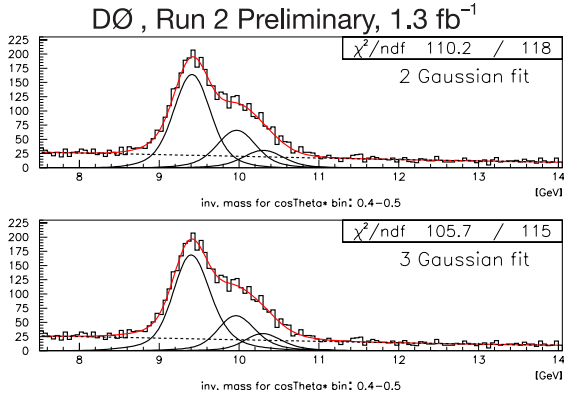


FIG. 14: The  $\mu^+\mu^-$  mass distribution at  $D\bar{0}$  after selection cuts, for one bin in  $|\cos\theta^*|$  and  $p_T$ , with  $|\cos\theta^*| \in [0.4, 0.5]$  and  $p_T \in [10 \text{ GeV}, 15 \text{ GeV}]$ . The plot shows the total fit to the data in red for the two fit models briefly described in the text, and the Gaussians describing the individual contribution of the  $\Upsilon(1S)$ ,  $\Upsilon(2S)$  and  $\Upsilon(3S)$ . The background fit is shown as a dotted line.

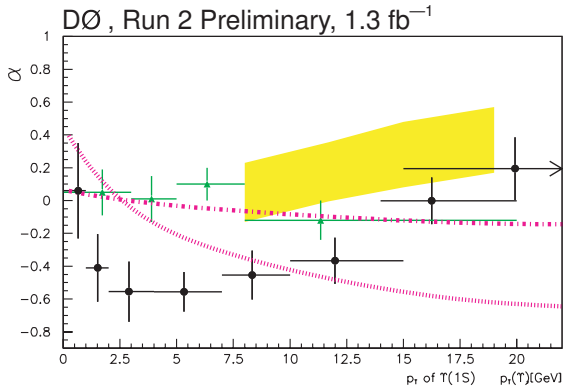


FIG. 15: The polarisation parameter  $\alpha$  versus  $p_T$  measured in  $\Upsilon(1S) \rightarrow \mu\mu$  events in  $1.3 \text{ fb}^{-1}$  of data at  $D\bar{0}$ . The measured results in eight  $p_T$  bins are shown as black circles with error bars. The yellow band corresponds the NRQCD prediction given in [52]. The magenta lines correspond to two limit cases of the  $k_T$ -factorisation model [46, 47]. The CDF Run I result [53] is shown as the green triangles with error bars.

and  $\Upsilon(3S)$ . Because of the relatively small number of  $\Upsilon(3S)$  events, to ensure a stable fit, the width, relative position and the fraction of events in the  $\Upsilon(3S)$  peak were taken from MC simulation and fixed in the fit. In another fit, the position of the  $\Upsilon(3S)$  peak is allowed to float. The difference between the two approaches is taken as a systematic error. The  $\Upsilon(1S)$  polarisation vs  $p_T$  is shown in Fig 15. The data represent the result for an admixture of directly produced  $\Upsilon(1S)$  and  $\Upsilon(1S)$  from other sources, in particular from  $\Upsilon(2S)$ ,  $\Upsilon(3S)$  and  $\chi_b$ . For comparison, the CDF Run I result is superimposed in the same plot, as well as theory predictions for the polarisation parameter  $\alpha$  of this admixture. The NRQCD prediction given in

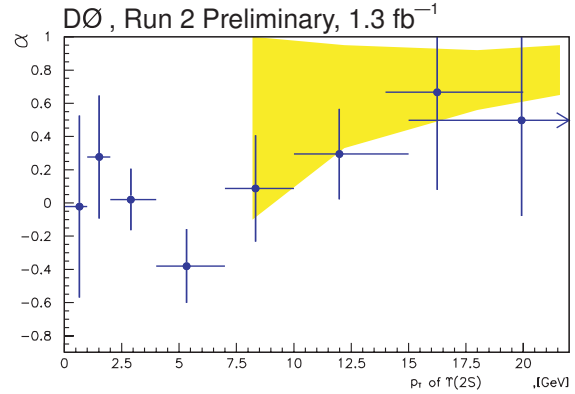


FIG. 16: The polarisation parameter  $\alpha$  versus  $p_T$  measured in  $\Upsilon(2S) \rightarrow \mu\mu$  events in  $1.3 \text{ fb}^{-1}$  of data at  $D\bar{0}$ . The data are shown as black circles with error bars. The yellow band shows the NRQCD prediction from [52].

[52] is shown as a yellow band, and two limit-cases of the  $k_T$ -factorisation model [46, 47] are given as magenta curves; the flatter of the two magenta curves corresponds to  $k_T$ -factorisation with the assumption of full quark-spin conservation, the steeper curve to full quark-spin depolarisation.  $D\bar{0}$  find clear evidence for longitudinal polarisation, in contradiction to the NRQCD calculation. The polarisation vs  $p_T$  in the statistically less powerful  $\Upsilon(2S)$  channel, which includes contributions from directly produced  $\Upsilon(2S)$  as well as feed-down from  $\Upsilon(3S)$  and  $\chi_b(2P)$ , is shown in Fig 16. In contrast to the result for the  $\Upsilon(1S)$ , the measured  $\Upsilon(2S)$  polarisation is compatible with NRQCD.

## VII. RELATIVE PRODUCTION CROSS SECTION $\chi_{c2}$ AND $\chi_{c1}$

The measurement of the  $\chi_{cJ}$  ( $J = 1, 2$ ) cross section is an interesting measurement in its own right, as well as important input to  $J/\psi$  production measurements to which it provides an important source of feed-down. Experimentally, this measurement has always been plagued by the poor mass resolution of the reconstructed  $\chi_{cJ}$  which is due to the soft photon in the decay chain  $\chi_{cJ} \rightarrow J/\psi\gamma$ . The high luminosity at the Tevatron now provides sufficient statistics to restrict the analysis only to events where the photon undergoes conversions to an  $e^+e^-$  pair. The momenta of the electrons can be measured precisely resulting in a far superior energy resolution of the photon than would be possible by measuring the photon's energy in the calorimeter. This leads to an excellent resolution of the reconstructed  $\chi_{cJ}$  mass, allowing a separation of the  $J = 0, 1, 2$  states. CDF reconstructs  $\chi_{cJ}$  in the channel  $\chi_{cJ} \rightarrow J/\psi(\mu\mu)\gamma(e^+e^-)$  within the kinematic range  $p_T(J/\psi) \in [4, 20] \text{ GeV}$ . To select photon

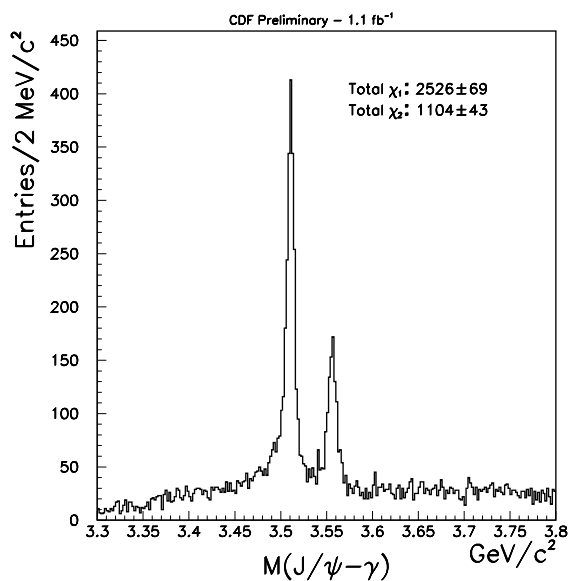


FIG. 17: Reconstructed  $\mu^+\mu^-(\gamma \rightarrow e^+e^-)$  mass, showing clearly two distinct mass peaks at the  $\chi_{c1}$  and  $\chi_{c2}$  mass.

conversions, the  $e^+e^-$  pair is a required to form a well-reconstructed vertex a large distance ( $> 12$  cm) from the beam, well inside the instrumented region of CDF. The spectrum of the  $(\mu^+\mu^-\gamma)$  invariant mass is shown in Fig 17, showing two well-separated peaks at the  $\chi_{c1}$  mass and the  $\chi_{c2}$  mass. No significant evidence for  $\chi_{c0}$  production can be seen. After all selection cut total number of  $\chi_{cJ} \rightarrow J/\psi(\mu\mu)\gamma(e^+e^-)$  events found in  $1.1\text{ fb}^{-1}$  is  $\sim 7k$ .

The distance between the beamline and the  $\mu^+\mu^-$  vertex is used to separate the prompt contribution from  $\chi_{cJ}$  originating from B decays. The measured ratio for prompt production is:

$$\frac{\sigma(\chi_{c2})}{\sigma(\chi_{c1})} = 0.70 \pm 0.04(\text{stat}) \pm 0.03(\text{sys}) \pm 0.06(\text{BF})$$

for  $p_T(J/\psi) \in [4, 20]$  GeV. The last contribution to

the error is due to the uncertainty in the branching fraction of  $\chi_{cJ} \rightarrow J/\psi\gamma$ . This result is at odds with the expectation from the colour octet model, which, by counting spin-states, predicts a ratio of  $5/3$ .

## VIII. CONCLUSIONS

The large charm and bottom production cross section at  $\sqrt{s} = 1.96$  TeV proton-antiproton collisions, combined with the capabilities of the DØ and the CDF detector provide the opportunity for new measurements with unprecedented statistics and precision.

In this paper we presented Run II results on single and correlated open charm and bottom production as well as quarkonium production and polarisation. The same theoretical framework that managed to describe successfully the unexpectedly large charmonium production cross observed at Tevatron Run I now fails to account for the significant longitudinal polarisation of charmonium and bottomium observed in Run II, nor the  $\chi_{c2}$  and  $\chi_{c1}$  cross section ratio. Several alternative models are being developed, but at the time of writing this paper, none has provided a detailed quantitative post-diction of the charmonium polarisation vs  $p_T$  that matches the observed data.

So heavy flavour production is, refreshingly, a field that is clearly led by experiment. In response to the data from the Tevatron, some of which have been presented here, we can look forward to new calculations and models, offering new descriptions of the mechanism of heavy flavour, and in particular quarkonium, production. We will also see further new measurements making use of the large amount of data yet to be analysed. Only about 1/3 of the Tevatron data taken so far have been used for the results presented here, and with the machine going stronger than ever, we can expect to at least double the integrated Tevatron luminosity before the end of Run II.

- 
- [1] D. E. Acosta et al. (CDF), Phys. Rev. **D65**, 052005 (2002), hep-ph/0111359.
  - [2] B. Abbott et al. (D0), Phys. Rev. Lett. **85**, 5068 (2000), hep-ex/0008021.
  - [3] F. Abe et al. (CDF), Phys. Rev. Lett. **79**, 572 (1997).
  - [4] M. Cacciari, M. Greco, and P. Nason, JHEP **05**, 007 (1998), hep-ph/9803400.
  - [5] V. M. Abazov et al. (D0), Nucl. Instrum. Meth. **A565**, 463 (2006), physics/0507191.
  - [6] D. E. Acosta et al. (CDF), Phys. Rev. **D71**, 032001 (2005), hep-ex/0412071.
  - [7] V. M. Abazov et al., Nucl. Instrum. Meth. **A552**, 372 (2005), physics/0503151.
  - [8] B. Ashmanskas et al. (CDF-II), Nucl. Instrum. Meth. **A518**, 532 (2004), physics/0306169.
  - [9] A. Abulencia et al. (CDF), Phys. Rev. Lett. **97**, 242003 (2006), hep-ex/0609040.
  - [10] D. E. Acosta et al. (CDF), Phys. Rev. Lett. **91**, 241804 (2003), hep-ex/0307080.
  - [11] M. Cacciari and P. Nason, JHEP **09**, 006 (2003), hep-ph/0306212.
  - [12] A. Abulencia et al. (CDF), Phys. Rev. **D75**, 012010 (2007), hep-ex/0612015.
  - [13] F. Abe et al. (CDF), Phys. Rev. Lett. **75**, 1451 (1995), hep-ex/9503013.
  - [14] P. Nason, S. Dawson, and R. K. Ellis, Nucl. Phys. **B327**, 49 (1989), erratum-ibid.B335:260,1990.
  - [15] W. Beenakker, W. L. van Neerven, R. Meng, G. A.

- Schuler, and J. Smith, Nucl. Phys. **B351**, 507 (1991).
- [16] M. Cacciari and P. Nason, Phys. Rev. Lett. **89**, 122003 (2002), hep-ph/0204025.
- [17] M. Cacciari, S. Frixione, M. L. Mangano, P. Nason, and G. Ridolfi, JHEP **07**, 033 (2004), hep-ph/0312132.
- [18] F. Happacher (2006), prepared for 14th International Workshop on Deep Inelastic Scattering (DIS 2006), Tsukuba, Japan, 20-24 Apr 2006.
- [19] D. Acosta et al. (CDF), Phys. Rev. **D69**, 072004 (2004), hep-ex/0311051.
- [20] C. Peterson, D. Schlatter, I. Schmitt, and P. M. Zerwas, Phys. Rev. **D27**, 105 (1983).
- [21] J. Chrin, Z. Phys. **C36**, 163 (1987).
- [22] T. Sjostrand, L. Lonnblad, and S. Mrenna (2001), hep-ph/0108264.
- [23] R. D. Field (CDF) (2002), hep-ph/0201192.
- [24] R. Field and R. C. Group (CDF) (2005), hep-ph/0510198.
- [25] R. D. Field (CDF) (2003), [http://www-cdf.fnal.gov/cdfnotes/cdf6403\\_UE\\_Run2.ps.gz](http://www-cdf.fnal.gov/cdfnotes/cdf6403_UE_Run2.ps.gz).
- [26] R. D. Field (CDF) (2002), rick Field's webpage with up-to-date information on Pythia Tune Set A.
- [27] V. A. Khoze, A. D. Martin, M. G. Ryskin, and W. J. Stirling, Eur. Phys. J. **C39**, 163 (2005), hep-ph/0410020.
- [28] R. Baier and R. Ruckl, Z. Phys. **C19**, 251 (1983).
- [29] B. Guberina, J. H. Kuhn, R. D. Peccei, and R. Ruckl, Nucl. Phys. **B174**, 317 (1980).
- [30] E. Braaten, M. A. Doncheski, S. Fleming, and M. L. Mangano, Phys. Lett. **B333**, 548 (1994), hep-ph/9405407.
- [31] E. Braaten and S. Fleming, Phys. Rev. Lett. **74**, 3327 (1995), hep-ph/9411365.
- [32] G. T. Bodwin, E. Braaten, and G. P. Lepage, Phys. Rev. **D51**, 1125 (1995), hep-ph/9407339.
- [33] H. Fritzsch, Phys. Lett. **B67**, 217 (1977).
- [34] F. Halzen, Phys. Lett. **B69**, 105 (1977).
- [35] J. F. Amundson, O. J. P. Eboli, E. M. Gregores, and F. Halzen, Phys. Lett. **B372**, 127 (1996), hep-ph/9512248.
- [36] J. F. Amundson, O. J. P. Eboli, E. M. Gregores, and F. Halzen, Phys. Lett. **B390**, 323 (1997), hep-ph/9605295.
- [37] P. Hagler, R. Kirschner, A. Schafer, L. Szymanowski, and O. V. Teryaev, Phys. Rev. **D63**, 077501 (2001), hep-ph/0008316.
- [38] E. Braaten, B. A. Kniehl, and J. Lee, Phys. Rev. **D62**, 094005 (2000), hep-ph/9911436.
- [39] S. Catani, M. Ciafaloni, and F. Hautmann, Phys. Lett. **B242**, 97 (1990).
- [40] S. Catani, M. Ciafaloni, and F. Hautmann, Nucl. Phys. **B366**, 135 (1991).
- [41] J. C. Collins and R. K. Ellis, Nucl. Phys. **B360**, 3 (1991).
- [42] G. Camici and M. Ciafaloni, Phys. Lett. **B386**, 341 (1996), hep-ph/9606427.
- [43] G. Camici and M. Ciafaloni, Nucl. Phys. **B496**, 305 (1997), hep-ph/9701303.
- [44] M. G. Ryskin, A. G. Shuvaev, and Y. M. Shabelski, Phys. Atom. Nucl. **64**, 120 (2001), hep-ph/9907507.
- [45] P. Hagler, R. Kirschner, A. Schafer, L. Szymanowski, and O. Teryaev, Phys. Rev. **D62**, 071502 (2000), hep-ph/0002077.
- [46] S. P. Baranov, Phys. Rev. **D66**, 114003 (2002).
- [47] S. P. Baranov and N. P. Zotov (2007), arXiv:0707.0253 [hep-ph].
- [48] J. P. Lansberg, Int. J. Mod. Phys. **A21**, 3857 (2006), hep-ph/0602091.
- [49] A. Abulencia et al. (CDF), Phys. Rev. Lett. **99**, 132001 (2007), hep-ex/0609040.
- [50] P. L. Cho and M. B. Wise, Phys. Lett. **B346**, 129 (1995), hep-ph/9411303.
- [51] M. Beneke and I. Z. Rothstein, Phys. Lett. **B372**, 157 (1996), hep-ph/9509375.
- [52] E. Braaten and J. Lee, Phys. Rev. **D63**, 071501 (2001), hep-ph/0012244.
- [53] D. E. Acosta et al. (CDF), Phys. Rev. Lett. **88**, 161802 (2002).